DOI: 10.15480/882.9303

Eighth International Symposium on Marine Propulsors
smp'24, Berlin, Germany, March 2024

Effects of Thickness Manufacturing Tolerance on Cavitation Performance of a Full-Scale Propeller

Shanqin Jin, Heather Peng and Wei Qiu*

Department of Ocean and Naval Architectural Engineering,
Memorial University of Newfoundland (MUN), St John's, NL, Canada

Email: qiuw@mun.ca

ABSTRACT

In this paper, effects of thickness manufacturing defects on the open-water cavitation performance of a full-scale propeller, based on the geometry of David Taylor Model Basin (DTMB) 5168 propeller, were studied with the 3-D steady Reynolds-Averaged Navier-Stokes (RANS) solver. The thickness manufacturing defects were distributed between the blade sections of r/R = 0.5 and r/R = 0.9. Three thickness deviations (0.5%, 1.0% and 2.0%) within ISO 484 Class S between $0.4c$ and $0.5c$ along the chord length were applied. Following the recommended best-practice settings for RANS simulations in previous studies on leading-edge (LE) defects, open-water simulations were conducted for full-scale propellers with and without thickness defects. The results indicated that maximum reduction in cavitation inception speed due to thickness manufacturing tolerances reached 7.48% for the investigated advance ratios.

Keywords

RANS, thickness manufacturing tolerances, cavitation performance, DTMB 5168 propeller.

1 INTRODUCTION

The majority of marine propellers manufactured today are hand- or robotic finished from castings which are rough machined using computer numerical control (CNC). Manual grinding of propeller surfaces introduces inaccuracies and deviations from design, which could lead to degradation of propeller performance in terms of cavitation, noise and efficiency.

Manufacturing tolerances for new ship propellers are specified by organizations, such as International Standards Organization (ISO), which defines the manufacturing standards for marine propeller. ISO (2015a) 484-1 applies to propellers with diameters greater than 2.5 m, while ISO (2015b) 484-2 is applicable to propellers with diameters ranging from 0.8 m to 2.5 m. Each standard categorizes tolerances into four distinct classes, each intended for specific types of vessels. Among the four classes, Class S represents the smallest tolerance and signifying the highest level of precision.

Many studies have been carried out to investigate the effects of design parameters on propeller performance with an object to mitigate vortex cavitation. For example, Peng et al. (2013) studied the tip vortex flow of a DTMB propeller model by using a commercial RANS solver ANSYS CFX. The study was further extended by Ali et al. (2017) to improve the grid generation for a spiral-like grid with relatively smaller first-grid spacing. For the concept design of propeller, Lafeber et al. (2022) employed a semi-empirical model to predict underwater radiated noise (URN) resulting from propeller cavitation. Remarkably, acceptable results were achieved with only the main propeller particulars as input parameters. Most recently, Stark (2023) investigated the effects of leading-edge (LE) tubercles on the vortex development of ducted propeller. It was showed that the application of LE tubercles led to improvements in both noise reduction and open-water performance. However, limited efforts have been made to address the influence of manufacturing tolerances on propeller performance. A preliminary computational fluid dynamics (CFD) study carried out by Hally (2008) indicated that the manufacturing defects potentially have large impact on propeller cavitation.

Extensive studies have been carried out by authors to understand the effects of LE defects on cavitation performance, including 2-D RANS simulations of foils with and without LE defects (Jin et al., 2020), 3-D RANS studies on foils of 1 m span (Jin et al., 2021), validation studies for foils of 0.525 m span (Zha et al., 2021), and 3-D RANS simulations of full-scale propellers with and without LE defects. The results showed that the LE defects within ISO 484 Class S tolerances narrow the cavitation buckets in the typical design range of angle of attack. LE defects can result in up to 40% reduction in cavitation inception speed.

Studies were extended to thickness defects in the present work. Since the thickness defects may exist anywhere on the blade surface, it is difficult to specify their sizes and locations on an actual propeller. Some simplifications were made in the present studies. The width of the region with thickness defects was set as $0.1c$. For the modified NACA 66 section (x/c = 0.45) studied in this work, it was assumed that the maximum thickness defect was near the location with the maximum thickness. Three thickness deviations (0.5%, 1.0% and 2.0%) within ISO 484 Class S were applied between $0.4c$ and $0.5c$ along the chord length. These thickness manufacturing defects were assumed to be distributed between the blade sections of r/R = 0.5 and r/R = 0.9. Following the best-practice settings of RANS simulations derived from our previous studies on LE defects, open-water simulations were carried out using the steady RANS solver in Star-CCM+ for full-scale propellers (with and without thickness defects) based on the geometry of DTMB 5168 propeller. The effects of thickness manufacturing defects on open-water and cavitation performance are presented and discussed.

2 THEORETICAL BACKGROUND

2.1 Governing Equations

The governing equations for the incompressible turbulence flow, satisfying the conservation of mass and conservation of momentum, are given below:

Continuity equation:

$$\frac{\partial \overline{u}_i}{\partial x_i} = 0 \tag{1}$$

Momentum equation:

$$\rho\frac{\partial \overline{u}_i}{\partial t} + \rho\frac{\partial \overline{u}_i\overline{u}_j}{\partial x_j} = \frac{\partial}{\partial x_j}\left[\mu\left(\frac{\partial \overline{u}_i}{\partial x_j}+\frac{\partial \overline{u}_j}{\partial x_i}\right) - \rho\overline{u_i'u_j'}\right] - \frac{\partial \overline{p}}{\partial x_i} + \rho g_i \tag{2}$$

where $\overline{u}_i$, i = 1, 2 and 3, denotes the mean velocity components along x-, y- and z-axis, respectively, $\overline{p}$ is the mean pressure, ρ is the density of the fluid, μ is the fluid dynamic viscosity, g_i is the acceleration of gravity, and $-\rho\overline{u_i'u_j'}$ is the term of Reynolds stress.

2.2 Turbulence Modeling

The Reynolds stresses can be solved based on the Boussinesq hypothesis using the eddy viscosity turbulence models, or be solved from the transport equation based on Reynolds stress models. In the eddy viscosity models, it is assumed that the Reynolds stresses are related to the mean velocity gradients, the turbulence kinetic energy and the eddy viscosity, i.e.,

$$-\rho\overline{u_i'u_j'} = \mu_t\left(\frac{\partial \overline{u}_i}{\partial x_j}+\frac{\partial \overline{u}_j}{\partial x_i}\right) - \frac{2}{3}\rho k\delta_{ij} \tag{3}$$

where μ_t represents the eddy viscosity, δ_{ij} is the Kronecker delta, $k = \frac{1}{2}\overline{u_i'u_j'}$ is the turbulent kinetic energy that can be solved from the transport equations.

It has been shown that two-equation turbulence models can provide sufficient accuracy in predicting ship hydrodynamic problems. Based on our previous studies (Jin et al., 2020, 2021), the $k - \omega$ model from Wilcox (2008) was applied in this work.

2.3 Geometry and computational domain

Simulations were conducted for propellers that have the same geometry as the five-bladed fixed-pitch propeller model, DTMB 5168. Detailed geometry and principal particulars of the DTMB 5168 propeller, in both model and full scales, are presented in Fig. 1 and Table 1, respectively. The Cartesian coordinate system is also shown in Fig. 1, where the origin is located at the center of propeller plane, the positive direction of X-axis is from upstream to downstream, and the positive direction of Z-axis is upward. For geometric simplification, a cylinder with constant radius (blue part) and with a cap (red part) was used to model the hub, and the root fillets were neglected. The geometry of the cap was defined by

$$\frac{(\mathrm{X}+0.3R)^2}{(0.65R)^2} + \frac{\mathrm{Y}^2}{(0.2819R)^2} + \frac{\mathrm{Z}^2}{(0.2819R)^2} = 1 \tag{4}$$

where the value of X is in the range of $-0.95\,R$ to $-0.30\,R$.

Table 1: The particulars for the five-bladed propeller DTMB 5168 (scale ratio = 5.71)

Item	Model	Full scale
Diameter of propeller, D, (m)	0.4027	2.2989
Radius of propeller, R, (m)	0.2013	1.1494
Diameter of hub, D_h, (m)	0.1135	0.6481
Chord length at 0.70 R, $c_{0.7}$, (m)	0.1752	1.0000
Maximum thickness at 0.70 R, $t_{0.7}$, (m)	0.0085	0.0487

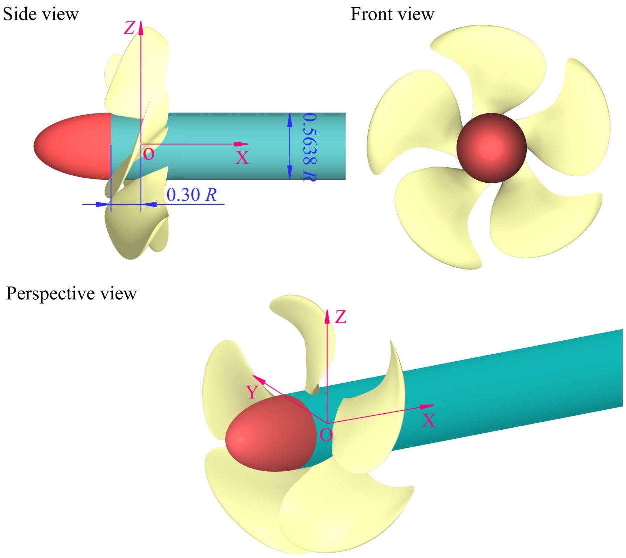

Figure 1: Geometry of propeller DTMB 5168

As shown in Fig. 2, the computational domain is composed of two cylindrical regions: a rotating part containing the propeller and a static part for the rest of the domain. The length of upstream is represented by L_up, L_down is the length of downstream, T_rp denotes the thickness of the rotating part, and D_sp and D_rp are the diameters of the static and the rotating parts, respectively. To simulate the rotating part, the Multiple Reference Frame (MRF) technique was employed. In terms of boundary conditions, velocity boundary conditions were imposed on the inlet while the pressure boundary conditions were specified at the outlet. The far field was set as a slip wall, and no-slip wall condition was applied on the surfaces of the propeller and other solid bodies in the domain.

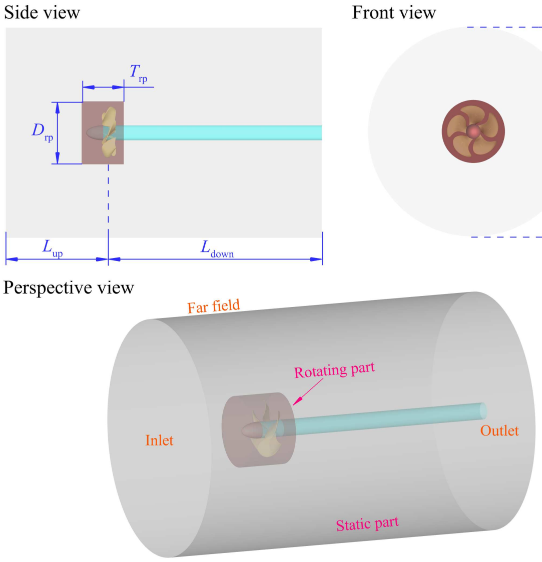

Figure 2: Computational domain

2.4 Thickness manufacturing defects

A thickness manufacturing defect is determined by measuring the difference between the designed and the manufactured blade sections. Table 2 summarizes the tolerances on the thickness of the blade section for various accuracy classes, where Class S is denoted as the highest precision in the ISO standards. It should also be noted that thickness defects cannot be modeled in simulations of the model-scale propeller since they are very small.

Three thickness defects, 0.5%, 1.0% and 2.0% (within ISO 484 Class S) between $0.4c$ and $0.5c$ along the chord length were studied. The details of thickness defects on various blade sections at $r/R = 0.5$, 0.6, 0.7, 0.8 and 0.9 are given in Table 3. They are very small compared to the thickness of their corresponding blade sections.

Table 2: Tolerances on the thickness of the blade section (ISO, 2015a, 2015b)

Specification	Class			
	S	I	II	III
Plus tolerances but not less than	+2.0% 2.0 mm	+2.5% 2.5 mm	+4.0% 4.0 mm	+6.0% 6.0 mm
Minus tolerances but not less than	-1.0% -1.0 mm	-1.5% -1.5 mm	-2.0% -2.0 mm	-4.0% -4.0 mm

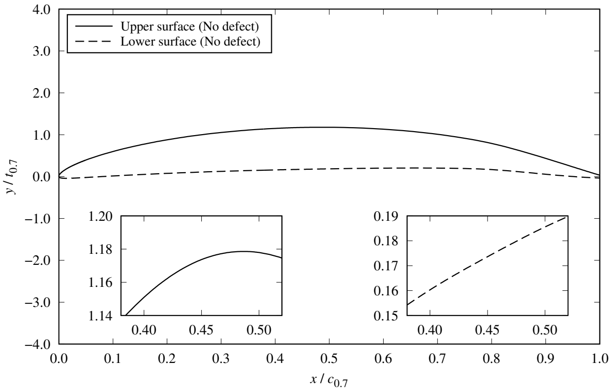

(a) No defect

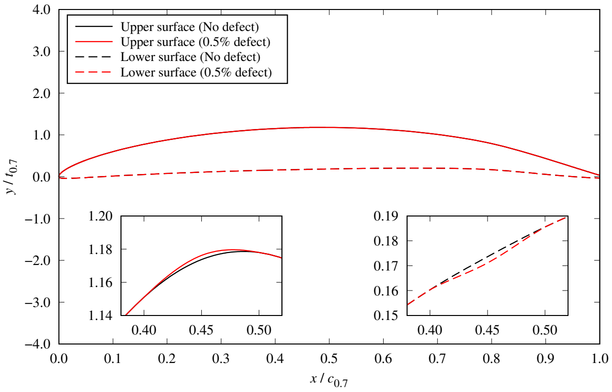

(b) 0.5% defect

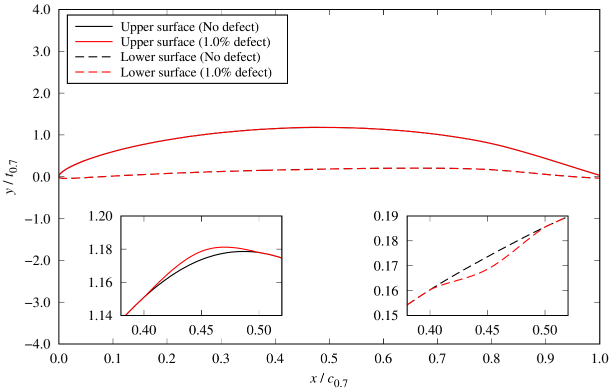

(c) 1.0% defect

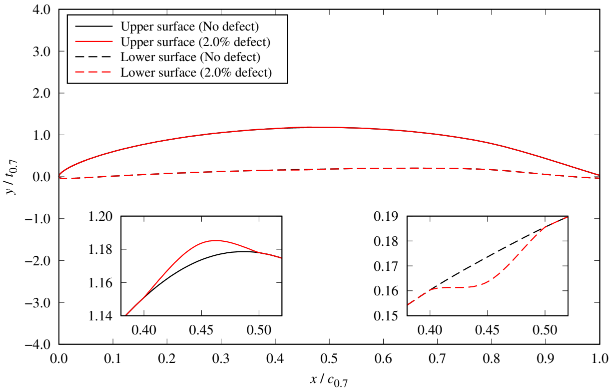

(d) 2.0% defect

Figure 3: Geometries for the full-scale propellers with and without thickness defects on the blade section of $r/R = 0.7$

For example, the geometric details of the full-scale propellers with and without thickness defects on the blade section of $r/R = 0.7$ are presented in Fig. 3. Note that the 3-D blade sections have been expanded into a local 2-D coordinate system which origin is located at the leading edge. Figure 4 shows the full-scale propeller with 2.0% defects. In the present study, the defects (purple parts) were distributed between the blade sections of $r/R = 0.5$ and $r/R = 0.9$.

Table 3: Dimensions of thickness tolerances on various blade sections (unit: mm)

r/R	Thickness, t	Thickness defect		
		0.5%	1.0%	2.0%
0.50	57.9568	0.2898	0.5796	1.1591
0.60	51.9005	0.2595	0.5190	1.0380
0.70	48.7400	0.2437	0.4874	0.9748
0.80	44.8103	0.2241	0.4481	0.8962
0.90	46.7779	0.2339	0.4678	0.9356

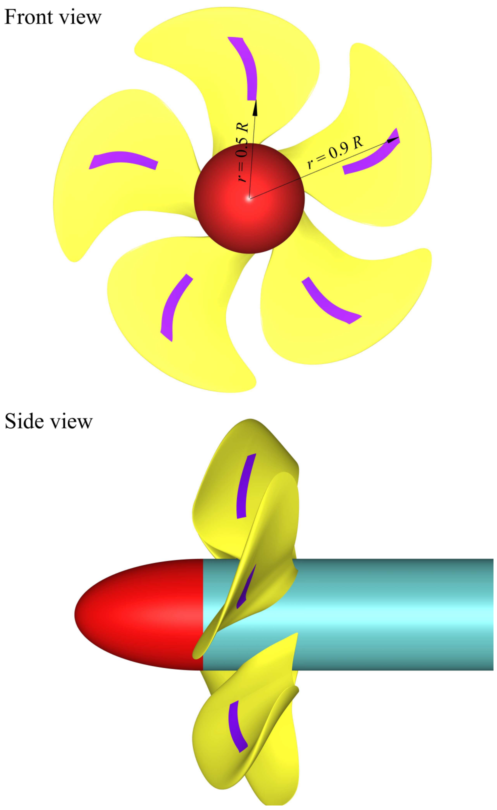

Figure 4: Geometry of the full-scale propeller with 2.0% defect

2.5 Grid generation

As an example, the blade surface mesh of the full-scale propeller with 2.0% defect is shown in Fig. 5. Structured grid was distributed on the blade surface, and the same number of grids was applied on both the pressure and suction sides. The hexahedron grids in the prism layer were then generated by extending the surface meshes along the wall's normal direction.

The first-grid spacing (ΔS) in terms of y^+ is estimated by

$$\Delta S = \frac{2y^+ c_{0.7}}{\mathrm{Re}\sqrt{0.5C_f}} \tag{5}$$

in which, the Reynolds number, Re, is determined by

$$\mathrm{Re} = \frac{c_{0.7}U_{0.7}}{\nu} = \frac{c_{0.7}\sqrt{{U_\infty}^2 + (0.7n\pi D)^2}}{\nu} \tag{6}$$

where $c_{0.7}$ and $U_{0.7}$ represent the chord length and the combined velocity of the blade section at 0.7 R, respectively, U_∞ is the incoming flow velocity in the open-water simulation, ν is the kinematic viscosity of water, n is the revolution speed, and D is diameter of the propeller.

The friction coefficient, C_f, is estimated using the ITTC 1957 formula (ITTC, 2021):

$$C_f = \frac{0.075}{(\log \mathrm{Re} - 2)^2} \tag{7}$$

The thickness of boundary layer, δ, is estimated by

$$\delta = 0.37\frac{c_{0.7}}{\mathrm{Re}^{1/5}} \tag{8}$$

Due to the large gradients of the velocity field within the tip vortices, a high grid resolution is required to accurately capture tip vortices over a distance. Figure 6 shows the grids on the downstream section of $X/R = 0.2386$. The bulge observed in Fig. 6 represents propeller blade surface with 2.0% defect. Such defects could be introduced through manual or robotic grinding in the actual manufacturing process. In present work, the cubic spline function was used to generate the deformation. The shapes of these defects might potentially be smoother when the other spline functions were employed. The grids were refined between the 0.9 R and 1.1 R in order to capture the tip vortices downstream. The mean cell size in the vortex refinement zone in terms of $\Delta x/D$ is 8.787E-4 in this figure.

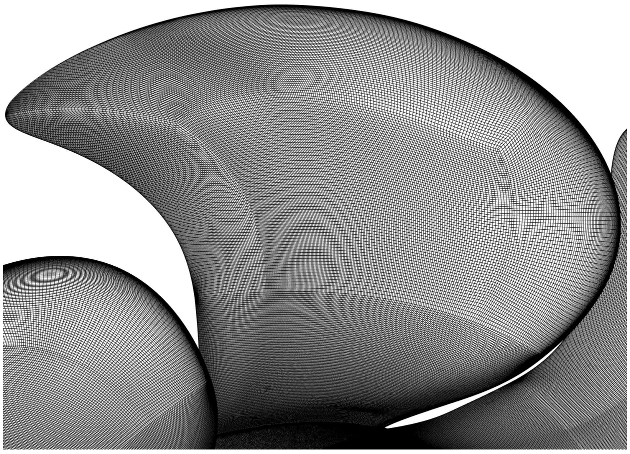

Figure 5: The blade surface mesh for the DTMB 5168 propeller with 2.0% thickness defect

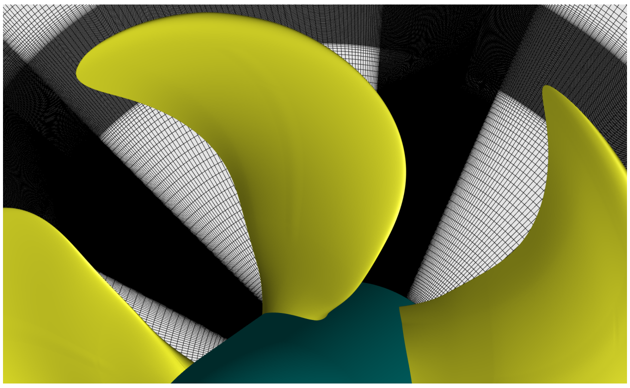

Figure 6: The grids on the downstream section at $X/R = 0.2386$

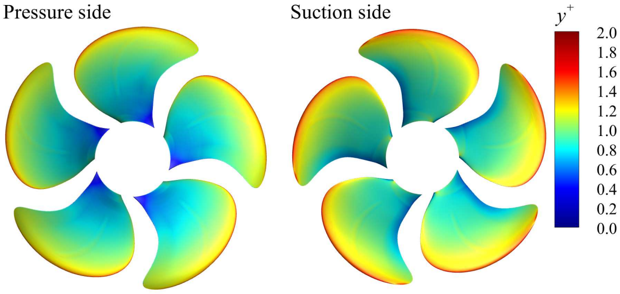

Figure 7: The distribution of calculated y^+ on the propeller blades with 2.0% thickness defect at J = 1.102

Following the best-practice settings derived from previous studies on LE defects, the target value of y^+ was set as 1.0 at the blade section of 0.7 R to resolve the flow in the boundary-layer, and 26 grids were applied on the thickness defect. For instance, Fig. 7 shows the distribution of calculated y^+ on the propeller blades with 2.0% thickness defect at J = 1.102. The average value of calculated y^+ was 0.98 in this case. The typical number of grids for the propellers without and with 0.5%, 1.0%, 2.0% thickness defects at the advance ratio of J = 1.102 are summarized in Table 4.

Table 4: Total number of grids for the full-scale propellers with no, 0.5%, 1.0% and 2.0% thickness defects at J = 1.102

Defect	Number of grids on defect	Total number of grids
No defect	-	146,261,855
0.5% defect	26	146,317,246
1.0% defect	26	146,361,777
2.0% defect	26	146,393,978

2.6 Non-dimensionalization and definition of variables

The relationships between the axial, tangential, and radial velocities (U_x, U_t and U_r) in the stationary frame and those in the rotating frame are given by:

$$\begin{aligned} V_x &= U_x \\ V_t &= U_t - 2\pi n r \\ V_r &= U_r \end{aligned} \tag{9}$$

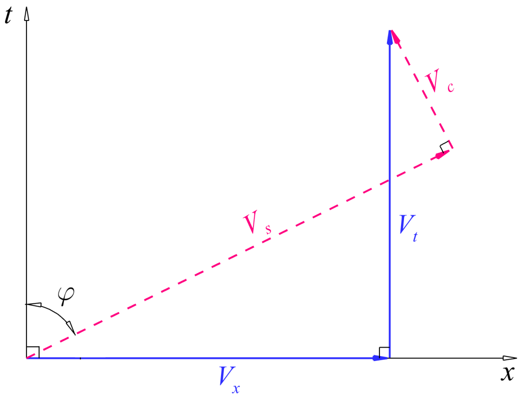

Figure 8: Primary and secondary coordinate system

where n is the propeller revolution speed, V_x, V_t and V_r are the axial, tangential, and radial velocities in the rotating frame, respectively. These velocities are all normalized by the incoming flow velocity, U_∞.

To provide a more comprehensive description of the tip vortex structure, a primary/secondary coordinate system, as shown in Fig. 8, is introduced. In this coordinate system, the primary velocity, V_s, is defined in the axial-tangential ($x - t$) plane at the propeller pitch angle, φ. The tangential velocity, V_c, and the radial velocity, V_r, are then defined on the secondary-flow plane ($r - c$ plane), which is perpendicular to the primary velocity. Note that the pitch angle varies with the radius of a section, and as a result, the coordinate systems are different at different radii. The relationships for these velocity components are expressed as follows:

$$\begin{aligned} V_s &= V_x \sin(\varphi) + V_t \cos(\varphi) \\ V_c &= V_t \sin(\varphi) - V_x \cos(\varphi) \\ V_r &= V_r \end{aligned} \tag{10}$$

The propeller thrust coefficient, K_{T}, and the torque coefficient, K_{Q}, are defined as follows,

$$K_{\mathrm{T}} = \frac{T}{\rho n^2 D^4} \quad \text{and} \quad K_{\mathrm{Q}} = \frac{Q}{\rho n^2 D^5} \tag{11}$$

where T and Q are the thrust and torque, respectively.

The propeller open-water efficiency, η_0, is given by

$$\eta_0 = \frac{J}{2\pi} \cdot \frac{K_{\mathrm{T}}}{K_{\mathrm{Q}}} \tag{12}$$

where $J = U_a/(nD)$ is the advance coefficient, and the advance speed, U_a, is equal to the incoming flow velocity, U_∞, in the open-water tests and simulations.

The pressure coefficient is defined as:

$$C_p = \frac{p - p_0}{0.5 \rho U_\infty^2} \tag{13}$$

where p is the absolute pressure, and p_0 is the reference static pressure,

$$p_0 = p_a + \rho g h \tag{14}$$

where p_a and ρgh denote the air and hydrostatic pressure, respectively.

The minimum pressure coefficient is defined as

$$C_{p_{\min}} = \frac{p_{\min} - p_0}{0.5\rho U_\infty^2} \tag{15}$$

where $p_{\min}$ is the the minimum pressure.

The cavitation number, σ, is defined as:

$$\sigma = \frac{p_0 - p_v}{0.5\rho U_\infty^2} \tag{16}$$

where p_v is the vapour pressure of water. Cavitation occurs if $-C_{p_{\min}} \geq \sigma$. The condition for cavitation inception is therefore $-C_{p_{\min}} = \sigma$.

Introducing the cavitation inception speeds, U_0 and U', for the sections without and with thickness defect, respectively, as follows:

$$U_0 = \sqrt{\frac{2(p_v - p_0)}{\rho C_{p_{\min}}}} \tag{17}$$

$$U' = \sqrt{\frac{2(p_v - p_0)}{\rho C'_{p_{\min}}}} \tag{18}$$

the cavitation inception speed ratio, ISR, is then defined as

$$\mathrm{ISR} = \frac{U'}{U_0} = \sqrt{\frac{C_{p_{\min}}}{C'_{p_{\min}}}} \tag{19}$$

where $C_{p_{\min}}$ and $C'_{p_{\min}}$ are the minimum pressure coefficients for the sections without and with thickness defect, respectively.

2.7 Simulation parameters

Extensive convergence studies have been conducted for the full-scale propellers, with and without LE defects, in previous studies. The best-practice settings for open-water simulation were summarized in Table 5. In this table, SR represents the grid stretch ratio of prism-layer, and $\Delta x/D$ denotes the grid size in the vortex refinement zone.

Using the recommended best practices, simulations were performed for the full-scale propellers with no, 0.5%, 1.0% and 2.0% thickness defects at various advance ratios ranging from 0.921 to 1.205. The same advance ratios and cavitation numbers were applied as those in the experimental cases (Chesnakas and Jessup, 1998). The detailed simulation parameters, such as the advance ratio, J, the propeller revolution speed, n, the incoming flow velocity, U_∞, and the static pressure, p_0, were summarized in Tables 6 and 7. Two static pressure conditions (p_0 = 16.5 psi and 22.0 psi) were simulated. Note that the static pressure, p_0, was measured at the same level of the centre of propeller shaft on the outlet. The model test results of K_T, $10K_\mathrm{Q}$, η_0 and σ by Chesnakas and Jessup (1998) are also included in these tables.

Table 5: The best-practice settings for open-water simulation with full-scale propeller

Item	Variable	Recommended value	Present setting
Static domain	L_up/D	$\geq$ 2.0	2.0
	L_down/D	$\geq$ 4.0	6.0
	D_sp/D	$\geq$ 6.0	6.0
Rotating domain	R_rp/R	$\geq$ 1.2	1.2
	T_rp/D	$\geq$ 0.8	0.8
Mesh size	SR	[1.1, 1.3]	1.2
	y^+	[0.5, 4.0]	1.0
	$\Delta x/D$	$\leq$ 6.212E-4	6.212E-4
Turbulence model		$k - \omega$ SST $k - \omega$	$k - \omega$

Table 6: The simulation matrix for suction-side tip vortex with p_0 = 16.5 psi

J	U_∞	n	Experimental (Model scale)			
	(m/s)	(rps)	K_T	$10K_\mathrm{Q}$	η_0	σ
1.004	7.621	3.302	0.349	0.852	0.654	3.860
1.059	9.608	3.947	0.322	0.806	0.674	2.430
1.115	10.709	4.178	0.299	0.755	0.703	1.950
1.136	11.816	4.525	0.290	0.736	0.714	1.600
1.159	13.166	4.942	0.278	0.710	0.722	1.290
1.205	15.480	5.588	0.241	0.653	0.707	0.930

Table 7: The simulation matrix for suction-side tip vortex with p_0 = 22.0 psi

J	U_∞	n	Experimental (Model scale)			
	(m/s)	(rps)	K_T	$10K_\mathrm{Q}$	η_0	σ
0.921	6.557	3.097	0.392	0.926	0.620	6.940
0.983	7.850	3.474	0.364	0.876	0.651	4.800
0.992	8.461	3.710	0.364	0.871	0.660	4.140
1.034	9.244	3.889	0.344	0.845	0.671	3.510
1.055	9.865	4.068	0.332	0.818	0.682	3.070
1.062	9.977	4.087	0.327	0.805	0.685	3.010
1.066	10.882	4.441	0.329	0.813	0.686	2.530
1.082	11.185	4.497	0.315	0.787	0.690	2.390
1.102	12.128	4.788	0.305	0.770	0.695	2.020
1.103	11.482	4.528	0.302	0.765	0.693	2.270
1.116	12.058	4.700	0.300	0.754	0.707	2.060
1.117	13.135	5.115	0.304	0.757	0.714	1.720
1.130	12.969	4.992	0.296	0.747	0.712	1.780
1.134	13.554	5.199	0.291	0.737	0.713	1.610
1.155	15.368	5.788	0.280	0.716	0.719	1.250
1.191	15.861	5.793	0.259	0.675	0.728	1.170
1.205	15.480	5.588	-	-	-	-

2.8 Convergence criteria

Two levels of convergence criteria were applied in the present studies, including:

- Residuals, defined as normalized root-mean-squared values in Star-CCM+, serve as the primary convergence criterion. An acceptable convergence level is achieved when residuals experience a three orders of magnitude reduction. Note that residuals are not the sole measure for convergence. The initial values can strongly influence the residuals, and if the initial solution already satisfies the discretized equations well, the residuals may not decrease significantly. Therefore, it is also necessary to examine the convergence of other parameters, i.e., pressure, thrust and torque coefficients.

- For the convergence of pressure, thrust and torque coefficients, the changes between their values at the present and previous iterations are used as indicators. The acceptable value is in the order of 10^{-4}.

The maximum number of iterations was set as 40,000 for all simulations. Residuals and changes in pressure, thrust and torque coefficients were then checked against the convergence criteria described above.

3 NUMERICAL RESULTS

Simulations were conducted using the best-practice settings provided in Table 5 for the full-scale propellers with and without thickness defects. Predicted residuals of simulation, open-water performance, downstream velocities, cavitation performance and the reduction of cavitation inception speed are presented and discussed in the following subsections. Since there is no available sea trial data for the full-scale propeller, experimental data from Chesnakas and Jessup (1998) of the propeller model are included in following figures as references. Note that the propeller in model scale has no defects.

3.1 Residuals

The normalized root mean squared values of residuals for all cells are employed to monitor the behavior of the solvers during each iteration in Star-CCM+. Figure 9 shows the residuals of simulations for the full-scale propellers with no defect, 0.5% defect, 1.0% defect, and 2.0% defect at $J = 1.102$ as an example. The legend in the figures provides information about the residuals for different equations, including "Continuity" for the continuity equation, "X momentum", "Y momentum" and "Z momentum" for the X-, Y-, Z-components of the momentum equation, "Tke" corresponds for the transport equation of turbulence kinetic energy (k), and "Sdr" for the transport equation of specific dissipation rate (ω). As seen in the figures, there is a reduction in three orders of magnitude in all residuals.

3.2 Open-water performance

The open-water performance of the full-scale propellers with and without thickness defects was examined at two static pressure (p_0 = 16.5 psi and 22.0 psi). The predicted thrust coefficients (K_T), torque coefficients (K_Q), and open-water efficiencies (η_0) for the full-scale propeller without defects at different static pressures are shown in Fig. 10. The results indicated that the influence of static pressure on the open-water performance is insignificant. The numerical results of the full-scale propellers without and with thickness defects at p_0 = 22.0 psi are presented in Fig. 11. It can be found that there is no significant difference in open-water performance for the propellers with and without thickness defects.

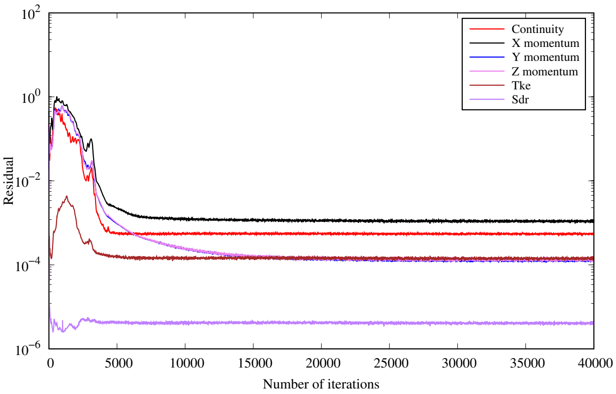

(a) No defect

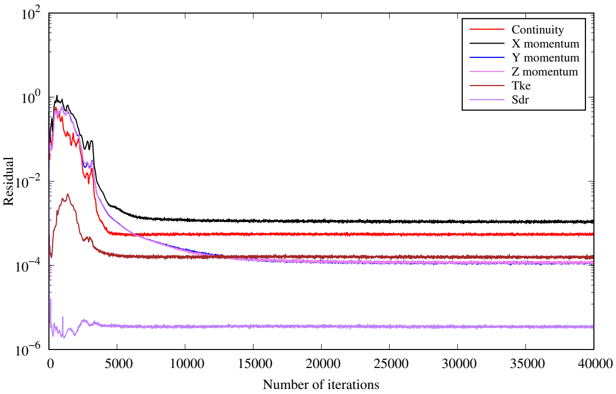

(b) 0.5% defect

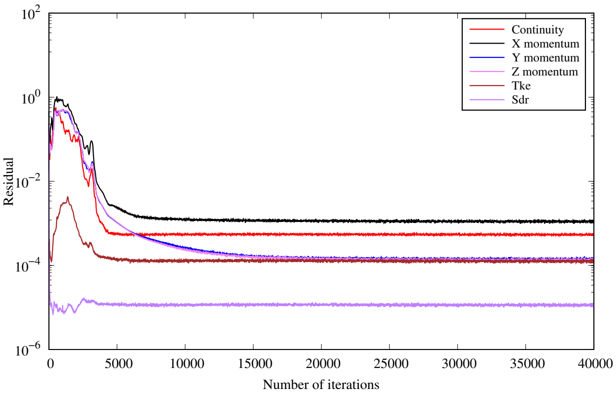

(c) 1.0% defect

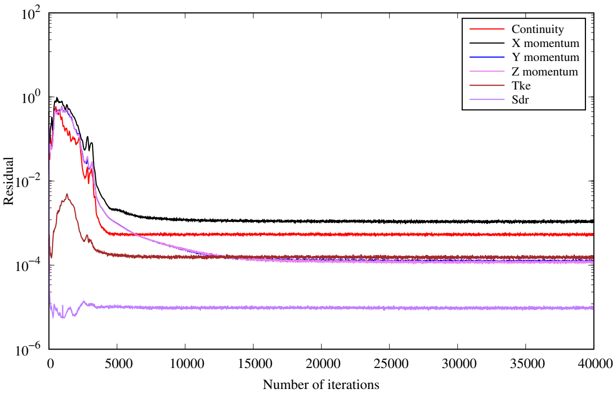

(d) 2.0% defect

Figure 9: Residuals of simulations for the full-scale propellers with and without thickness defects at $J = 1.102$

In comparison with predictions for the full-scale propeller without thickness defect, relative errors were calculated for the full-scale propellers with defects to further quantify differences in open-water performance. Figure 12 presents the calculated relative errors at two static pressures of p_0 = 16.5 psi and 22.0 psi. It is evident that the predicted K_T and K_Q are increased due to the presence of defects, with a larger thickness defect leading to greater increase in K_T and K_Q. All the relative errors are below 1.0%, and the maximum relative errors for K_T and K_Q (0.70% and 0.91%) are for the 2.0% thickness defect at J = 1.205 and p_0 = 16.5 psi. Due to the increased torque being greater than that of thrust, the open-water efficiency is decreased. As expected, the maximum reduction in efficiency (−0.21%) was found for the 2.0$ thickness defect at J = 1.205 and p_0 = 16.5 psi.

3.3 Downstream flow velocities

To validate the prediction of the tip vortex, a close-up view of the tip vortex at $X/R = 0.2386$ and $J = 1.102$ is presented in Fig. 13. In this study, the position of the vortex center is specified at $\theta = 0$, where the minimum pressure occurs within the tip vortex. The primary velocity is normalized with the inflow velocity in the rotating frame ($V_\infty = \sqrt{U_\infty^2 + 2\pi rn}$). Compared with the experimental data from Chesnakas and Jessup (1998) and the numerical solution of Hsiao and Pauley (1999), the predicted non-dimensional primary velocity, V_s/V_∞, in the tip vortex region of full-scale propeller with no defect was greater. The predicted tip vortex core of full-scale propeller without defect was located at $r/R = 0.927$, while the observed location of the tip vortex core was at $r/R = 0.920$ in the model experiment (Chesnakas and Jessup, 1998).

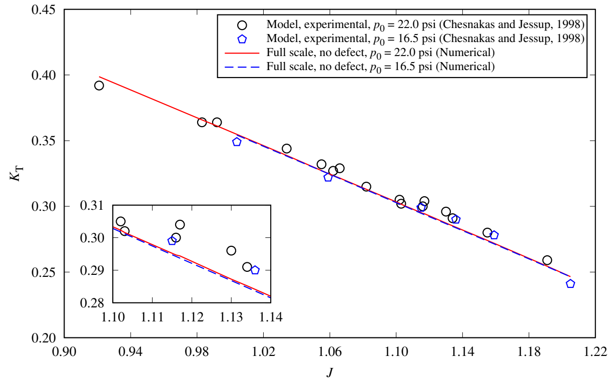

(a) Thrust coefficient, K_T (No defect)

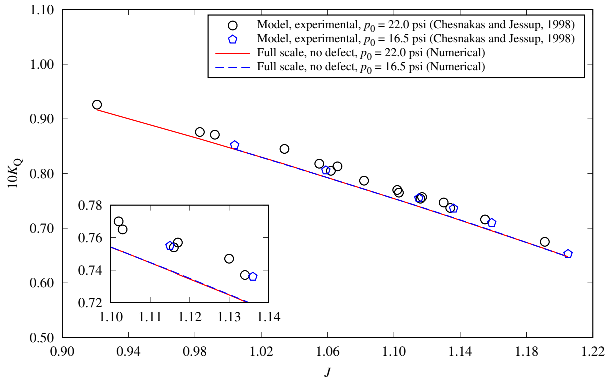

(b) Torque coefficient, K_Q (No defect)

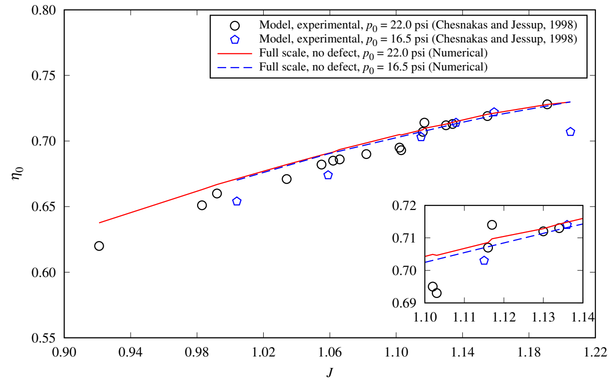

(c) Efficiency, η_0 (No defect)

Figure 10: Predicted open-water performance of the full-scale propeller with no defect at different static pressures

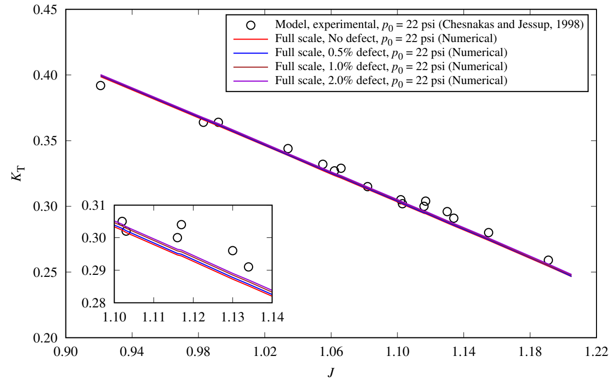

(a) Thrust coefficient, K_T

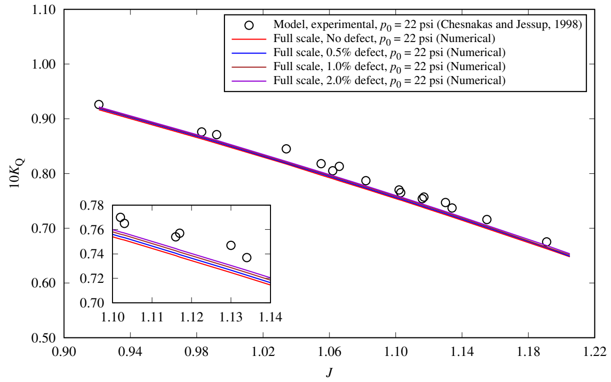

(b) Torque coefficient, K_Q

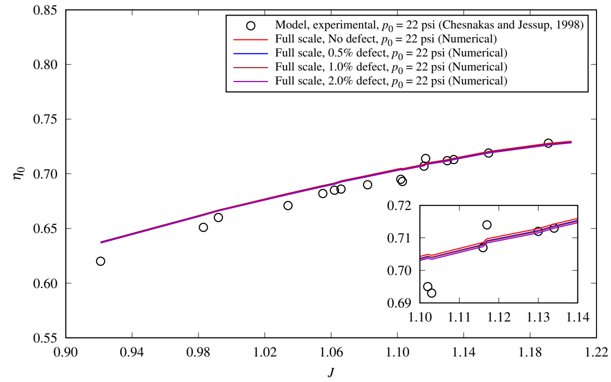

(c) Efficiency, η_0

Figure 11: Predicted open-water performance of the full-scale propellers without and with thickness defects at p_0 = 22.0 psi

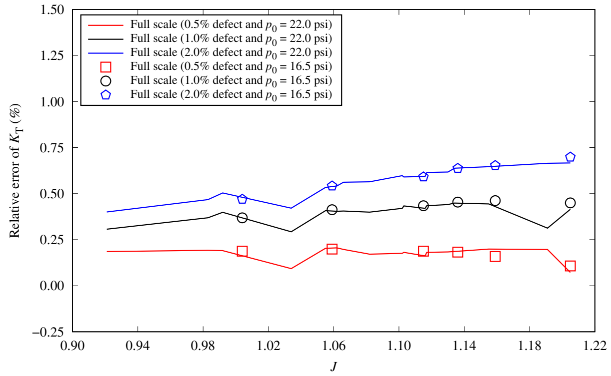

(a) Thrust coefficient, K_{T}

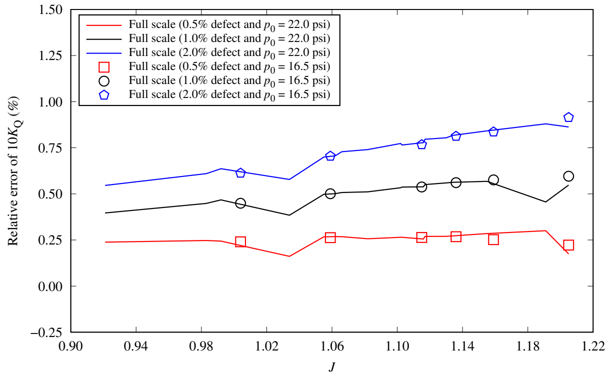

(b) Torque coefficient, K_{Q}

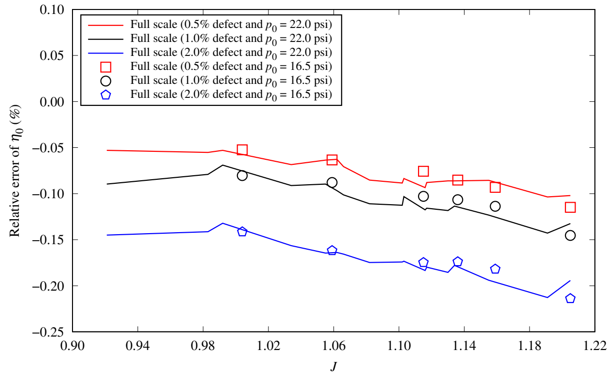

(c) Efficiency, η_0

Figure 12: The relative errors of open-water performance between the full-scale propellers without and with thickness defects

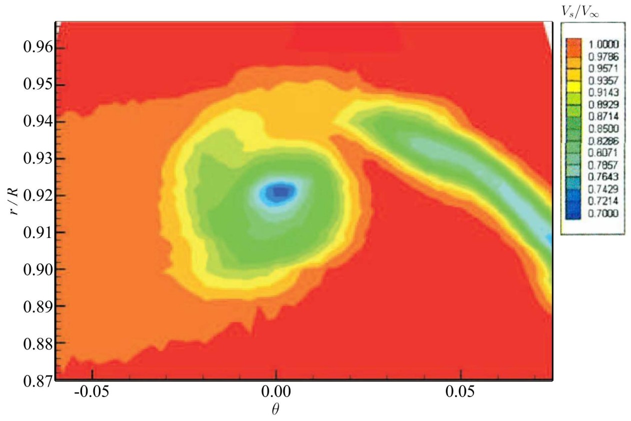

(a) Model, experimental (Chesnakas and Jessup, 1998)

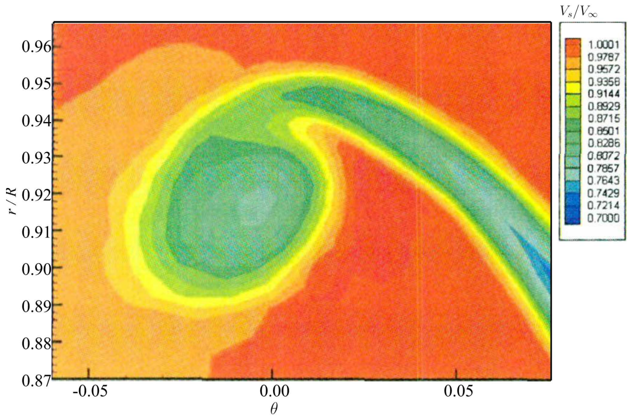

(b) Model, numerical (Hsiao and Pauley, 1999)

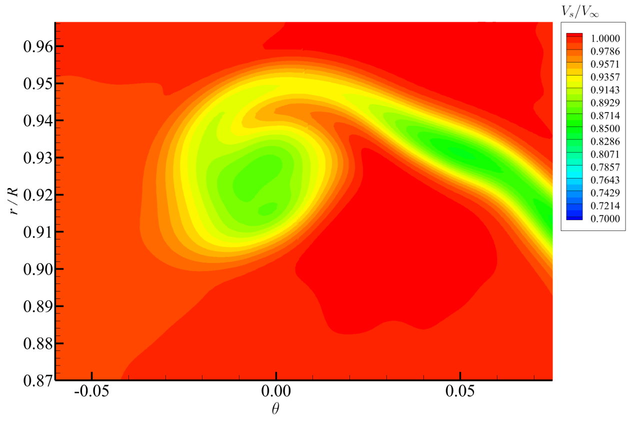

(c) Full scale, numerical (No defect)

Figure 13: Comparison of V_s/V_∞ in the tip vortex for the propeller at $X/R = 0.2386$ and $J = 1.102$

The primary velocity fields of full-scale propellers with and without thickness defects are shown in Fig. 14. In addition, the comparisons of three velocity components (V_x/U_∞, V_t/U_∞ and V_r/U_∞) for the basic case, $J = 1.102$, at downstream section of $X/R = 0.2386$ are presented in Figs. 15 to 17. It should be noted that the model experimental data (Chesnakas and Jessup, 1998) did not include the flow information near the hub. Slightly greater axial velocity predicted for the full-scale propeller led to a larger primary velocity within the vortex core region. It can also be found that the computed velocity fields with different thickness defects are visually similar to each other.

To further provide a comprehensive comparison between the numerical results of full-scale propellers and the model experimental data (Chesnakas and Jessup, 1998), the non-dimensional axial, tangential and radial velocities (V_x/U_∞, V_t/U_∞ and V_r/U_∞) in the rotating frame at $X/R = 0.1756$ and 0.2386 are presented in Figs. 18 and 19, respectively. Note that the averaged velocities across the five vortex cores were used. In these figures, the first valley, starting from the left, corresponds to the wake, while the second trough is associated with the tip vortex. It can be seen that both the axial and tangential velocities were greater within the downstream tip vortex region at $X/R = 0.1756$ and 0.2386. The results showed that the thickness

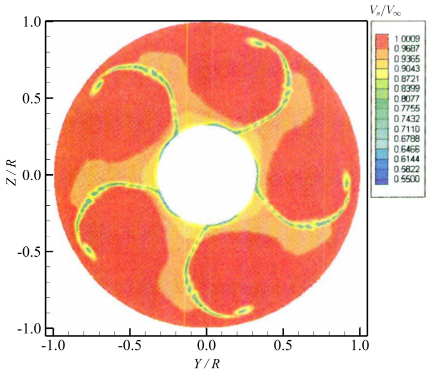

(a) Model scale (Chesnakas and Jessup, 1998) (b) Full scale (No defect)

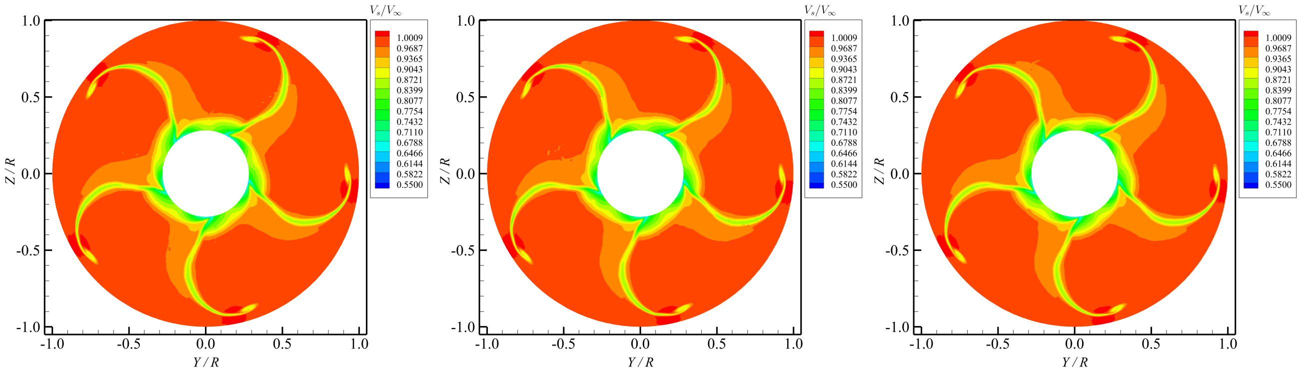

(c) Full scale (0.5% defect) (d) Full scale (1.0% defect) (e) Full scale (2.0% defect)

Figure 14: Comparison of contours of non-dimensional primary velocity, V_s/V_∞, at $X/R = 0.2386$ and $J = 1.102$ for the full-scale propellers with and without thickness defects

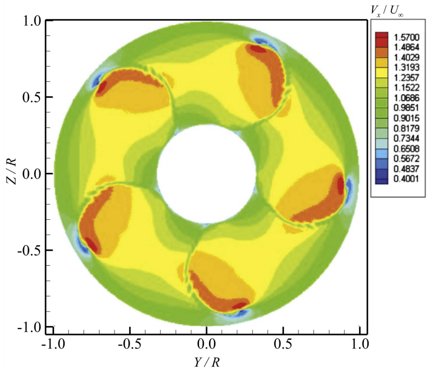

(a) Model scale (Chesnakas and Jessup, 1998) (b) Full scale (No defect)

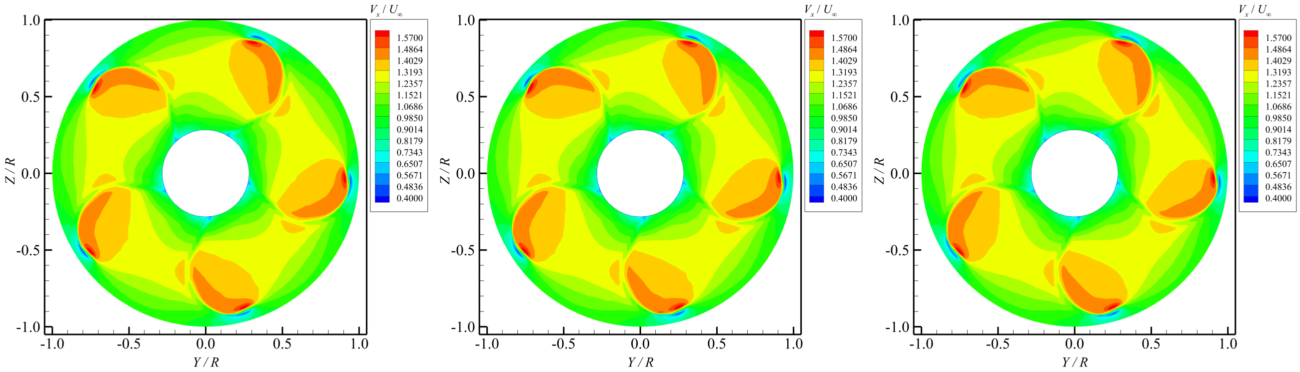

(c) Full scale (0.5% defect) (d) Full scale (1.0% defect) (e) Full scale (2.0% defect)

Figure 15: Comparison of contours of non-dimensional axial velocity, V_x/U_∞, at $X/R = 0.2386$ and $J = 1.102$ for the full-scale propellers with and without thickness defects

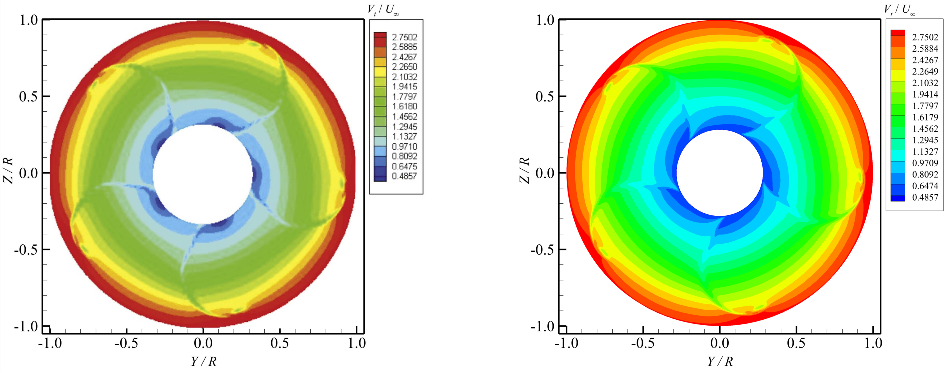

(a) Model scale (Chesnakas and Jessup, 1998)

(b) Full scale (No defect)

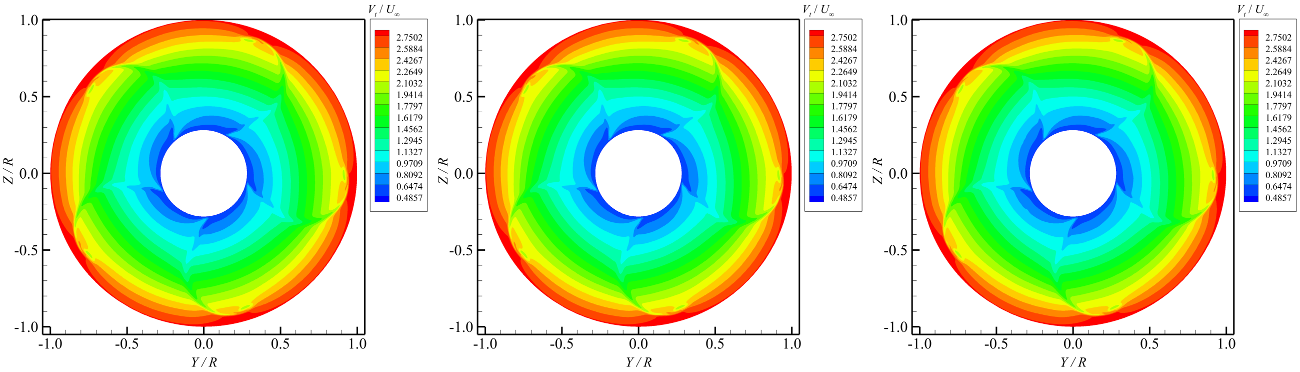

(c) Full scale (0.5% defect)

(d) Full scale (1.0% defect)

(e) Full scale (2.0% defect)

Figure 16: Comparison of contours of non-dimensional tangential velocity, V_t/U_∞, at $X/R = 0.2386$ and $J = 1.102$ for the full-scale propellers with and without thickness defects

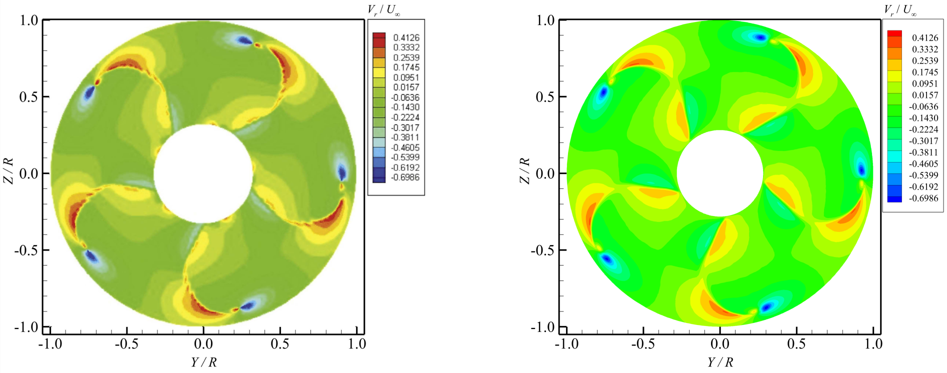

(a) Model scale (Chesnakas and Jessup, 1998)

(b) Full scale (No defect)

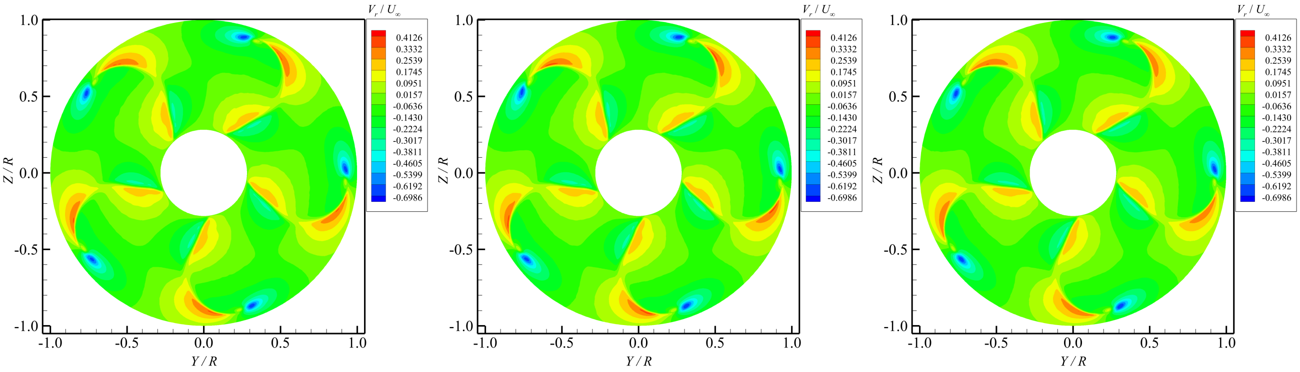

(c) Full scale (0.5% defect)

(d) Full scale (1.0% defect)

(e) Full scale (2.0% defect)

Figure 17: Comparison of contours of non-dimensional radial velocity, V_r/U_∞, at $X/R = 0.2386$ and $J = 1.102$ for the full-scale propellers with and without thickness defects

defects had no significant influence on the velocities across the tip vortex core.

3.4 Cavitation performance

The cavitation numbers on the blade sections of $r/R \in [0.5, 0.9]$ for the full-scale propellers without and with thickness defects are presented in Fig. 20. As expected, the predicted cavitation numbers on the blade sections with thickness defects show similarity at two static pressures. Minor discrepancies can be observed between the full-scale propellers without defect and with 2.0% defect when J is greater than 1.0, and the cavitation number decreases as the size of the defect decreases.

3.5 Effect of thickness defect on cavitation inception speed

Based on the predicted cavitation numbers shown in Fig. 20, Fig. 21 presents the comparison of the reduction percentages in cavitation inception speed on the blade sections of $r/R \in [0.5, 0.9]$ for the full-scale propellers with thickness defects. The calculation details for cavitation inception speed reduction ratios (ISR) are further provided in Table 8. From the predicted cavitation numbers and reductions in cavitation inception speed, it can be observed that the effect of thickness defect is relatively small on the blade sections of $r/R \in [0.5, 0.9]$.

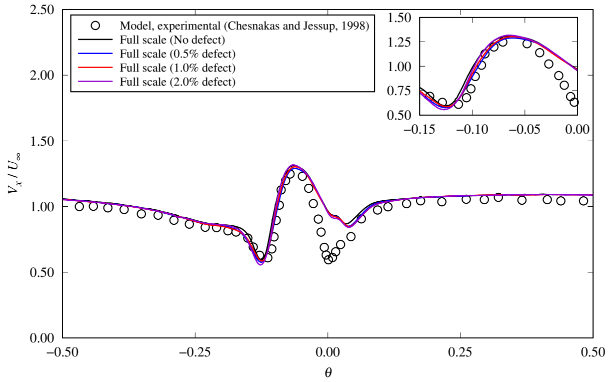

(a) Non-dimensional axial velocity, V_x/U_∞

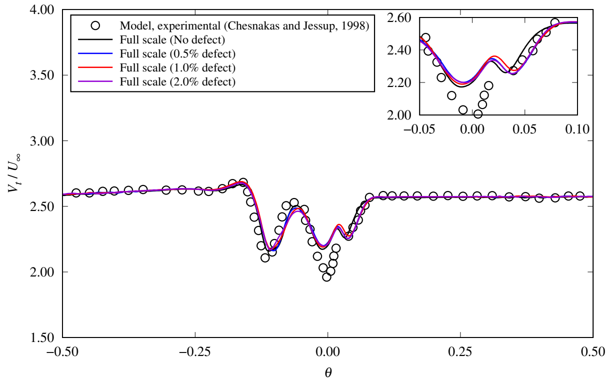

(b) Non-dimensional tangential velocity, V_t/U_∞

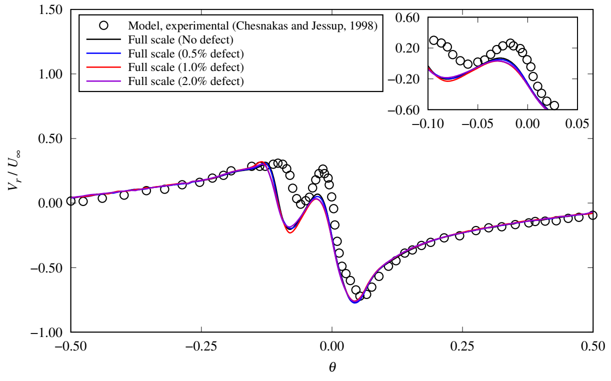

(c) Non-dimensional radial velocity, V_r/U_∞

Figure 18: Predicted V_x/U_∞, V_t/U_∞ and V_r/U_∞ across the vortex core at $X/R = 0.1756$ and $J = 1.102$

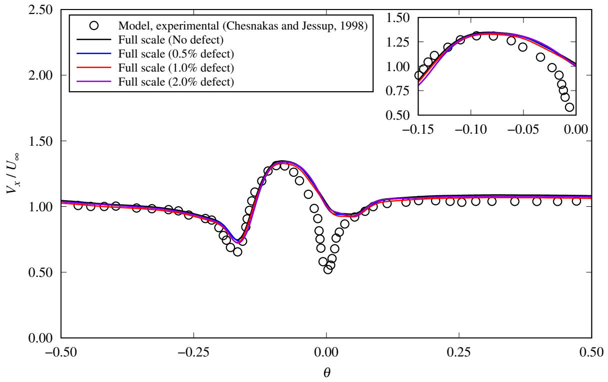

(a) Non-dimensional axial velocity, V_x/U_∞

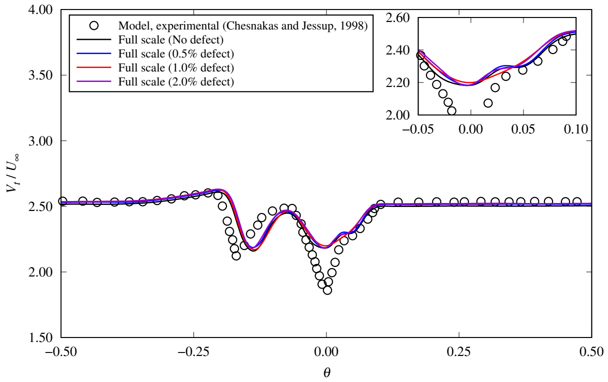

(b) Non-dimensional tangential velocity, V_t/U_∞

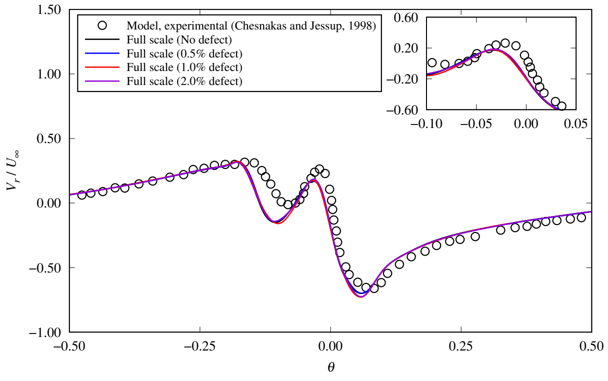

(c) Non-dimensional radial velocity, V_r/U_∞

Figure 19: Predicted V_x/U_∞, V_t/U_∞ and V_r/U_∞ across the vortex core at $X/R = 0.2386$ and $J = 1.102$

Table 8: Calculation details for the reduction in cavitation inception speed on the blade sections of $r/R \in [0.5, 0.9]$

p_0 (psi)	J	$-C_{p_{\min}}$				Percentage reduction in inception speed (%)		
		No defect	0.5% defect	1.0% defect	2.0% defect	0.5% defect	1.0% defect	2.0% defect
22.0	0.921	3.18942	3.16452	3.16214	3.15856	-0.39	-0.43	-0.49
	0.983	1.80289	1.79723	1.79899	1.80162	-0.16	-0.11	-0.04
	0.992	1.66265	1.66330	1.67288	1.68726	0.02	0.31	0.73
	1.034	1.34830	1.42958	1.47497	1.54307	2.88	4.39	6.52
	1.055	1.27518	1.37373	1.41502	1.47697	3.65	5.07	7.08
	1.062	1.26021	1.35494	1.39526	1.45573	3.56	4.96	6.96
	1.066	1.25239	1.34956	1.38781	1.44518	3.67	5.00	6.91
	1.082	1.21991	1.30707	1.34348	1.39810	3.39	4.71	6.59
	1.102	1.18385	1.26062	1.29358	1.34303	3.09	4.34	6.11
	1.103	1.18161	1.25528	1.28880	1.33909	2.98	4.25	6.06
	1.116	1.15960	1.22664	1.25792	1.30485	2.77	3.99	5.73
	1.117	1.15868	1.22855	1.25858	1.30364	2.89	4.05	5.72
	1.130	1.13752	1.19763	1.22626	1.26920	2.54	3.69	5.33
	1.134	1.13163	1.19022	1.21867	1.26134	2.49	3.64	5.28
	1.155	1.10093	1.14850	1.17585	1.21687	2.09	3.24	4.88
	1.191	1.50010	1.50312	1.60062	1.74687	0.10	3.19	7.33
	1.205	1.76408	1.77693	1.87337	2.06104	0.36	2.96	7.48
16.5	1.004	1.52615	1.53713	1.57910	1.64205	0.36	1.69	3.59
	1.059	1.26638	1.36064	1.40202	1.46408	3.53	4.96	7.00
	1.115	1.16082	1.22202	1.25547	1.30564	2.54	3.84	5.71
	1.136	1.12765	1.17882	1.20817	1.25219	2.19	3.39	5.10
	1.159	1.09422	1.13410	1.16001	1.19887	1.77	2.88	4.46
	1.205	1.75491	1.77682	1.87303	2.01734	0.62	3.20	6.73

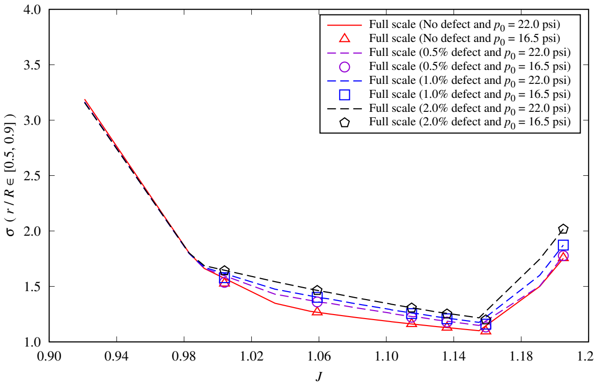

Figure 20: Cavitation numbers on the blade sections of $r/R \in [0.5, 0.9]$ for the full-scale propellers without and with thickness defects

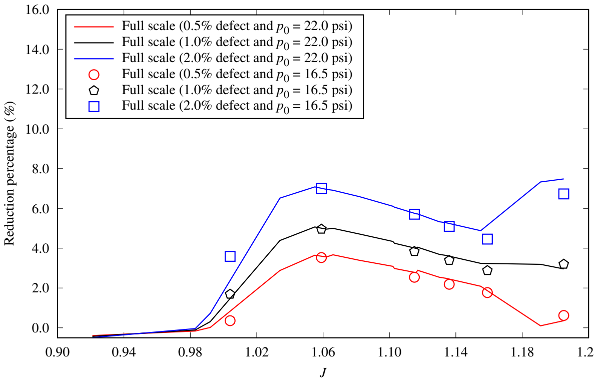

Figure 21: Reduction percentages in cavitation inception speed on the blade sections of $r/R \in [0.5, 0.9]$ for the full-scale propellers without and with defects

For the full-scale propeller with 2.0% thickness defect, the reduction in cavitation inception speed can reach to 7.48% at the advance ratio of $J = 1.205$ and the static pressure of 22.0 psi. Within the advance ratio ranging from 0.992 to 1.205, the reduction increases with the size of thickness defect increases. In summary, such thickness defects within ISO 484 Class S would lead to a minor reduction in the cavitation inception speeds at the investigated advance ratios.

4 CONCLUSION

Using the recommended best-practice settings for RANS simulations from previous studies on leading-edge (LE) defects, open-water simulations were carried out for full-scale propellers, based on the geometry of DTMB 5168 propeller, with and without thickness defects. Three thickness deviations (0.5%, 1.0% and 2.0%) within ISO 484 Class S between $0.4c$ and $0.5c$ along the chord length were examined. Theses thickness defects were distributed between the blade sections of $r/R = 0.5$ and $r/R = 0.9$. Simulations were performed with two static pressure conditions ($p_0 = 16.5$ psi and 22.0 psi) at the advance ratios ranging from 0.921 to 1.205. The results indicated that the influences of static pressure on the predictions were insignificant. The maximum reduction in cavitation inception speed was 7.48% for the full-scale propeller with 2.0% thickness defect at $J = 1.205$ and $p_0 = 22.0$ psi. Compared with the effect of leading-edge defects (Jin et al., 2020, 2021), the thickness manufacturing defect within ISO 484 Class S has less impact on the open-water and cavitation performance of a full-scale propeller.

ACKNOWLEDGMENTS

This work was supported by the Natural Science and Engineering Research Council (NSERC) of Canada.

REFERENCES

Ali, M. A., Peng, H., Qiu, W. & Bensow, R. (2017). ‘Prediction of propeller tip vortex using OpenFOAM’. Proceedings of the 36th International Conference on Ocean, Offshore and Arctic Engineering, Trondheim, Norway.

Chesnakas, C. J. & Jessup, S. D. (1998). ‘Cavitation and 3-D LDV tip-flow field measurements of propeller 5168’. Naval Surface Warfare Center Carderock Division Bethesda MD Hydromechanics Directorate, USA.

Hally, D. (2008). ‘Preliminary CFD simulations of 2-D foils with defects’. DRDC Atlantic Centre, Canada.

Hsiao, C. T. & Pauley, L. L. (1999). ‘Numerical computation of tip vortex flow generated by a marine propeller’. ASME Journal of Fluids Engineering, **121**(3), pp. 638–645.

ISO (2015a). ‘Shipbuilding – Ship screw propellers – manufacturing tolerances – Part 1: Propellers of diameter greater than 2.5 m’.

ISO (2015b). ‘Shipbuilding – Ship screw propellers – manufacturing tolerances – Part 2: Propellers of diameter between 0.80 and 2.5 m inclusive’.

ITTC (2021). ‘Recommended procedures and guidelines 7.5-02-02-01, resistance tests’. Proceedings of the 29th International Towing Tank Conference, Virtual.

Jin, S., Zha, R., Peng, H., Qiu, W. & Gospodnetic, S. (2020). ‘2D CFD studies on effects of leading-edge propeller manufacturing defects on cavitation performance’. SNAME Maritime Convention.

Jin, S., Zha, R., Peng, H. & Qiu, W. (2021). ‘Comparison of 2-D and 3-D RANS studies on effects of leading-edge propeller manufacturing defects on cavitation performance’. Proceedings of the 29th Annual Conference of the Computational Fluid Dynamics Society of Canada, St. John’s, Newfoundland and Labrador, Canada.

Lafeber, F. H., Bosschers, J., Lidtke, A., Lloyd, T., van Wijngaarden, E. & Moulijn, J. (2022). ’Prediction of underwater radiated noise from propeller cavitation during concept design’. Proceedings of the 7th International Symposium of Marine Propulsors, Wuxi, China.

Peng, H., Qiu, W. & Ni, S. (2013). ‘Effect of turbulence models on RANS computation of propeller vortex flow’. Ocean Engineering, **72**, pp. 304–317.

Stark, C. (2023). ‘Ducted propeller underwater radiated noise mitigation through leading-edge tubercle modifications’. Doctoral Dissertation, University of Strathclyde, Glasgow, Scotland.

Wilcox, D. C. (2008). ‘Formulation of the k-w turbulence model revisited’. AIAA Journal, **46**(11), pp. 2823–2838.

Zha, R., Jin, S., Peng, H. & Qiu, W. (2021). ‘Comparable studies on effects of leading-edge propeller manufacturing defects on cavitation performance’. Proceedings of the 29th Annual Conference of the Computational Fluid Dynamics Society of Canada, St. John’s, Newfoundland and Labrador, Canada.